Formation Dirac point and the topological surface states for HgCdTe-QW and mixed 3D HgCdTe TI

Michał Marchewka*

Faculty of Mathematics and Natural Sciences, Centre for Microelectronics and Nanotechnology, University of Rzeszów, Pigonia 1, 35-959 Rzeszów, Poland

Abstract. In this paper the results of numerical calculations based on the finite difference method (FDM) for the 2D and 3D TI with and without uniaxial tensile strain for mixed $Hg_{1-x}Cd_xTe$ structures are presented. The numerical calculations were made using the 8x8 model for x from 0 up to 0.155 and for the wide range for the thickness from a few nm for 2D up to 150 nm for 3D TI as well as for different mismatch of the lattice constant and different barrier potential in the case of the QW. For the investigated region of the Cd composition (x value) the negative energy gap ($E_g=\Gamma_8-\Gamma_6$) in the $Hg_{1-x}Cd_xTe$ is smaller than in the case of pure HgTe which, as it turns out, has a significant influence on the topological surface states (TSS) and the position of the Dirac point for QW as well as for 3D TI. The results show that the strained gap and the position of the Dirac point against the Γ_8 is a function of the x-Cd compounds in the case of the 3D TI as well as the critical width of the mixed $Hg_{1-x}Cd_xTe$ QW.

1 Introduction

In recent years, several different materials - topological insulators (TI) for which the topological surface states (TSS) were theoretically and experimentally confirmed have been identify. Starting from the 3D Bi-based materials e.g[1-5], through two dimensional (2D) systems based on HgCdTe/HgTe[6-8] up to strained 3D HgTe layers [9-11] all of these materials represent the new class of the quantum matter for which the metallic states exist on the surfaces. In all of these materials the conduction band is lower than the valence band which is caused by strong spin-orbital coupling. For all of these materials the TSS arise for different reasons [12,13]. The Dirac like dispersion is observed due to the potential of the 6.4 nm wide HgTe-QW in case of the CdTe/HgTe heterostructures. For 3D HgTe the uniaxial strain along (001) axis lifts the degeneracy of the Γ^8 band by breaking the cubic symmetry at the Γ-point and opens the insulating gap which makes such systems as 3D TI.

For 2D heterostructures as well as for the 3D TI based on the II-VI compounds like HgCdTe the eight band kp model is used for calculation the energy dispersion e.g [6,8,9,11,14-18]. This paper shows that the finite difference method (FDM) applied for 8×8 kp model [19,20] to solve numerical the differential Schrödinger equation gives an opportunity to analyse 2D and 3D structures which allows for creative design structures containing the so-called Dirac point and, what is important from the point of view of application possibilities - the shape of the Topological Protested Surface States (TPSS) [18].

For the two dimensional structures the experimental and the theoretical papers are devoted for the pure HgTe material as a material of the quantum wells. These structures are very good defined and the magneto optics and magetotransport properties have been investigated for a wide range of widths the HgTe-quantum well. For the mixed HgCdTe QW there is only a few papers which are dedicated such structures [21].

Similar case is for the 3D TI systems – the difference of the lattice constant between HgTe and the CdTe which is about 0.3% is enough to observe the TPSS and such structures are very popular e.g [9,18]. As for the 2D systems the 3D TI based on the HgTe are very popular and so far there is not so many papers devoted for 3D TI mixed HgCdTe [22].

There is still a few question e.g how to improve the 2D as well as the 3D structures to get the better properties of the electron transport through the interface/surface. For the 2D system the wider widths then 6.4 nm of the quantum wells seems to be better for such discussion. The detailed experiment were done for the 2D systems but for HgTe QW at different temperatures [23]. In the case of the 3D TI the situation is more complicated because the strained energy gap induced by the lattice mismatch is rather small (about 22meV) and only applied the external voltage it is possible to observe the dominating effects in electron transport thought the surface [18].

In this paper the results of numerical calculations for the unstrained and strained 2D and 3D (001) growth oriented mixed $Hg_{1-x}Cd_xTe$ structures are presented. The numerical calculations were made using the 8x8 kp model [19] for x from 0 up to 0.155 and for

* Corresponding author: marmi@ur.edu.pl

© The Authors, published by EDP Sciences. This is an open access article distributed under the terms of the Creative Commons Attribution License 4.0 (http://creativecommons.org/licenses/by/4.0/).

the different thickness (for QW and 3D TI-from 75 to 150 nm) as well as for a different mismatch of the lattice constant. For this region of the x-Cd composition the Γ^6 band approaching the degenerated $\Gamma_{hh}{}^8$ and $\Gamma_{lh}{}^8$ bands up to the values of the Eg = 0 (for x= 0.17 (at 4.2 K)) and for the 4um wide fully relaxed 3D crystal the Dirac like dispersion of the Γ^6 and $\Gamma_{lh}{}^8$ is expected [24]. Such structure with the unaxial strain for the investigated width region (up to 150 nm) is still strained [25]. The results for the dispersion relation for the typical 6.4 nm wide HgTe-QW as well as for the strained 75 nm wide HgTe structures obtained by the presented method are in a good the agreement with the results reported earlier [6,11,18].

As is presented below for the $Hg_{1-x}Cd_xTe$ unstrained quantum wells the critical widths is different for different x-Cd compounds as wells as in the well region as in the barrier materials. For the strained and wider than 6.4 nm 2D structures the electronic structures under the proper strain and x-Cd compounds looks like for the 3D TI based on mixed HgCdTe.

In the case of the 3D TI the numerical results show that the Dirac point can be found in the gap induced by strain in $Hg_{1-x}Cd_xTe$ structures with different x-Cd composition (for which the band structures are still inverted) and wider than in the earlier studies by other authors. The analysis of the dispersion relation for the 3D strained $Hg_{1-x}Cd_xTe$ layers is supplemented by the calculation of the dispersion relation for HgTe with a bigger unaxial strain than the one which usually comes from the different lattice constant between HgTe and CdTe. We demonstrate that the Dirac cone in 3D 75 nm wide HgTe cannot be found inside the indirect strained gap, not even for the bigger strain up to 2.3%. The combination of the different than zero x-Cd composition together with the bigger than 0.3% mismatch of the lattice constant between the substrate and the strained layers allow to get the dispersion relation of the TSS for 75 nm wide layers similar to those ones obtained for CdTe/HgTe QW with the most welcome position of the Dirac point inside the indirect isolating gap - a bit above the top of the $\Gamma_{hh}{}^8$ band.

2 Theory

2.1. Eight band kp model

The $Hg_{1-x}Cd_xTe$/HgTe QW are the heterostructures of type III[26] which depending on the width of the QW have normal or an inverted subband structures. For such materials the 8×8 kp model[19] (including spin splitting) allow, with successes, interpret a lot of experimental data. Because Schröodinger equation with the energy dependent effective mass with nonlinear eigenvalue problem cannot be solved directly, a few numerical methods (transfer matrix method[27-29], the shooting method[30], finite element method (FEM)[31] or FDM[32-35] have been proposed to solve the non-parabolic Schrödinger equation.

Numerical results presented in this paper were obtained using the 8x8 kp [19,20] model defined for (001) growth oriented structures. Originally, this model was applied to the quantum wells based on II-VI zinc-blende structures. In the presented kp model an eight band description of the band structure including all second-order terms representing the remote-band contributions with the J= +/- 3/2 - heavy hole and light hole bands – J=+/- 1/2 along with the J=+/- 1/2 conduction band states and J=+/-1/2 spin-orbit split off states are considered.

The Schröodinger equation for 8×8 Hamiltonian for the two dimensional vector of envelope functions, can be simply written as:

$$H\,\Psi(r) = E\,\Psi(r) \qquad (1)$$

where for such system the carrier wave-function can be written as:

$$\Psi(r) = \sum_n F_n(r)u_n(r). \qquad (2)$$

The $F_n(r)$ are the envelope function and the sum index of n varies from 1 to 8. The $u_n(r)$ are Bloch functions which are the same in the barrier and the well layers. F_n can be represented as

$$F_n = \exp\left[i\left(k_x x + k_y y\right)\right] f_n(z) \qquad (3)$$

where k_x and k_y are the wave vector components in the plane of the QW. Energy levels and envelope-function coefficients can be found from the simultaneous solution of the system of coupled differential equations. The Hamiltonian in such system takes the following form:

$$H_0 = \begin{bmatrix} T & 0 & -\frac{1}{\sqrt{2}}k_+P & \sqrt{\frac{2}{3}}k_zP & \frac{1}{\sqrt{6}}k_-P & 0 & -\frac{1}{\sqrt{3}}k_zP & -\frac{1}{\sqrt{3}}k_-P \\ 0 & T & 0 & -\frac{1}{\sqrt{6}}k_+P & \sqrt{\frac{2}{3}}k_zP & \frac{1}{\sqrt{2}}k_-P & -\frac{1}{\sqrt{3}}k_+P & \frac{1}{\sqrt{3}}k_zP \\ -\frac{1}{\sqrt{2}}k_-P & 0 & U+V & -\bar{S}_- & R & 0 & \frac{1}{\sqrt{2}}\bar{S}_- & -\sqrt{2}R \\ \sqrt{\frac{2}{3}}k_zP & -\frac{1}{\sqrt{6}}k_-P & -\bar{S}_-{}^\dagger & U-V & C & R & \sqrt{2}V & -\sqrt{\frac{3}{2}}\bar{S}_- \\ \frac{1}{\sqrt{6}}k_+P & \sqrt{\frac{2}{3}}k_zP & R^\dagger & C^\dagger & U-V & \bar{S}_+{}^\dagger & -\sqrt{\frac{3}{2}}\bar{S}_+ & -\sqrt{2}V \\ 0 & -\frac{1}{\sqrt{2}}k_+P & 0 & R^\dagger & \bar{S}_+ & U+V & \sqrt{2}R & \frac{1}{\sqrt{2}}\bar{S}_+ \\ -\frac{1}{\sqrt{3}}k_zP & -\frac{1}{\sqrt{3}}k_-P & \frac{1}{\sqrt{2}}\bar{S}_-{}^\dagger & \sqrt{2}V & -\sqrt{\frac{3}{2}}\bar{S}_+ & \sqrt{2}R & U-\Delta & C \\ -\frac{1}{\sqrt{3}}k_+P & \frac{1}{\sqrt{3}}k_zP & -\sqrt{2}R^\dagger & -\sqrt{\frac{3}{2}}\bar{S}_-{}^\dagger & -\sqrt{2}V & \frac{1}{\sqrt{2}}\bar{S}_+{}^\dagger & C^\dagger & U+\Delta \end{bmatrix} \qquad (4)$$

where

$$k_{||}^2 = k_x^2 + k_y^2;\ k_\pm = k_x \pm k_y;\ k_z = -\frac{i\partial}{\partial z};$$

$$T = E_c(z) + \frac{\hbar^2}{2m_0}\left[(2F+1)k_{||}^2 + k_z(2F+1)k_z\right]$$

$$U = E_v(z) - \frac{\hbar^2}{2m_0}\left(\gamma_1 k_{||}^2 + k_z\gamma_1 k_z\right)$$

$$V = -\frac{\hbar^2}{2m_0}\left(\gamma_2 k_{||}^2 + 2k_z\gamma_2 k_z\right)$$

$$R = -\frac{\hbar^2}{2m_0}\sqrt{3}(\mu k_+^2 - \bar{\gamma}k_-^2)$$

$$\bar{S}_\pm = -\frac{\hbar^2}{2m_0}\sqrt{3}k_\pm(\{\gamma_3, k_z\} + [\kappa, k_z])$$

$$\tilde{S}_\pm = -\frac{\hbar^2}{2m_0}\sqrt{3}k_\pm\left(\{\gamma_3, k_z\} - \frac{1}{3}[\kappa, k_z]\right)$$

$$C = \frac{\hbar^2}{2m_0}k_-[\kappa, k_z] \qquad (5)$$

[A,B]=AB-BA is the usual commutator and {A,B}=AB+BA is the anticommutator for the operators A and B; P is the Kane momentum matrix element;
$E_c(z)$ and $E_v(z)$ are the conduction and valence band edges, respectively; Δ is the spin-orbit splitting energy; γ_1, γ_2, γ_3, κ and F describe the coupling to the remote bands and the μ and $\bar{\gamma}$ are parameters according to $\mu=(\gamma_3-\gamma_2)/2$ and $\bar{\gamma}=(\gamma_3+\gamma_2)/2$. The band structure parameters for HgTe and CdTe used in calculations are listed in Table I. The dependence of the band gap for

$Hg_{1-x}Cd_xTe$ as a function of the temperature and composition x is determined from the empirical expression according to C. R. Becker et al. [27]. The valence band offset between HgTe and CdTe is taken to be equal to 570 ± 26 meV at T=5 K [27]. In the calculation is used 570 meV. The strain tensor components for an arbitrary growth direction can be determined by using the model of De Caro et al. [37]. The effects of the strain tensor can be incorporated in the Kane model through the Bir-Pikus Hamiltonian[38], which can be easily obtained from the Kane Hamiltonian with the substitution $k_i k_j \rightarrow \varepsilon_{ij}$. The shape of the Bir-Pikus Hamiltonian used in the calculations has been described in detail by E. G. Novik[20]. The strain tensor ε_{ij} for (001) growth direction has three values different than 0: $\epsilon_{11}, \epsilon_{22}$ and ϵ_{33} where $\epsilon_{11} = \epsilon_{22} = \epsilon_{33} = \epsilon_{||}$, and $\epsilon_{33} = -2\varepsilon C_{12}/C_{11}$. The lattice mismatch is defined as $\epsilon = (a_{CdTe} - a_{HgTe})/(a_{HgTe})$, and for the HgTe it is about 0.3%. The band gap between Γ_{hh}^8 and Γ_{lh}^8 is about 22 meV at k=0 due to the value of ϵ for (001) for the strained HgTe structure. The lattice constant of $Hg_{1-x}Cd_xTe$ as a function of x was taken as[39]: $a = 6.4614 + 0.008x + 0.01168x^2 - 0.0057x^3$ (in terms of angstroms). The mismatch of the lattice constant is the main element which affects a size of the gap for the $Hg_{1-x}Cd_xTe$ for which the Cd composition is between the studied region (which is about is about 20 meV see Fig. 1). In Fig. 1 the strained energy gap as a function of the x-Cd compounds are presented in two cases: green curves shows the approximation of the Eg(x-Cd) as a function of a(x) only while the red curves presents the Eg(x-Cd) when the Eg is a function of lattice constant as wells as the confection of the deformation potential and the stiffness constants. In the investigated region of x-Cd compounds (0 - 0.155 see inset) the Eg can be fitted using the approximation plotted by the green curve.

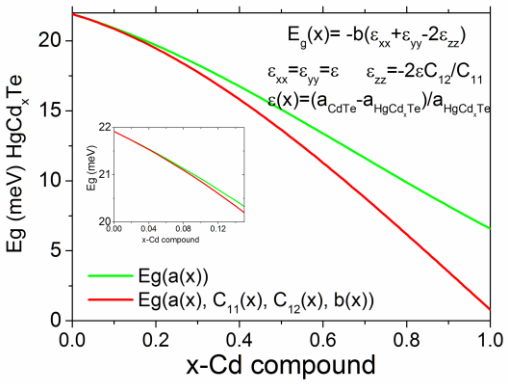

Fig. 1. The strained gap (between Γ_{hh}^8 and Γ_{lh}^8) as a function of: the lattice constant (green curve) only and the confection of the deformation potential and the stiffness constants (red curve) for the different x-Cd compounds

The results presented below were received for the band structure parameters collected in Table 1. Besides the coupling to the remote bands parameters (see above) we have: a, b, d -the Bir-Pikus deformation potential[38]; C, C_{11}, C_{22}, C_{44} - the stiffness constants. All presented results were calculated for 4.2 K and for the $k_{||} = (k_x, 0)$.

Table 1. The parameters used in calculations

	E_g	E_v	Δ	$E_p=2m_0P^2/\hbar^2$	F	γ_1	γ_2	γ_3	κ
HgTe	-0.303 eV	0	1.08 eV	18.8 eV	0	4.1	0.5	1.3	-0.4
CdTe	1.606 eV	-570 meV	0.91 eV	18.8 eV	-0.09	1.47	-0.28	0.03	-1.31

3 Results

3.1. Quantum wells

All presented results for quantum wells are obtained for the case when both barriers are about 100 nm which in practice means infinite potential. To get the better agreement with the real structures of the QW three different region were taken into account in the numerical calculation (see fig. 2): the CdTe layer (70 nm) and the buffer layer $Hg_{0.3}Cd_{0.7}Te$ (30 nm) which are placed for both sides of the different width of the HgTe-QW.

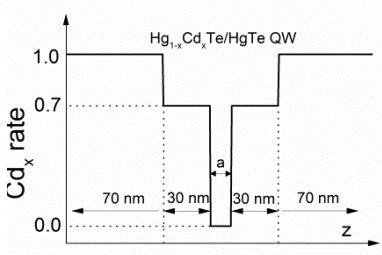

Fig. 2. The shape of potential of the investigated QW structures.

The distance between nearest two points Δz were defined to be equal half of the lattice constant of a unit cell. The dependencies of all parameters, except the band-gap, on the content of the solid solution $Hg_{1-x}Cd_xTe$ are assumed to be linear in x. To verify the validity of our proposed method and find the application range of this approach, the dispersion relation energy spectrum for different width of the QW were calculated.

The dispersion relation for the potential profile presented in Fig. 3 were calculated for two direction of k: $k_{||} = [10]$and $k_{||} = [11]$ HgTe QW for different values of the width of the QW and the results are presented in Fig. 4.

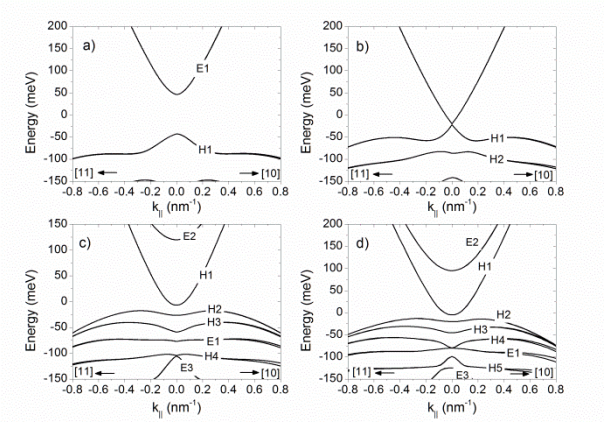

Fig. 3. Energy spectrum of size-quantized subbands in a symmetric CdTe/ $Hg_{0.3}Cd_{0.7}Te$/HgTe QW for a) 4nm, b) 6nm, c) 12nm, d) 14nm – wide QW calculated by FDM method applying for 8x8 kp Kane Hamiltonian for: $k_{||} = [10]$and $k_{||} = [11]$.

It can be clearly seen that our results are in good agreement with this presented in the literature by others authors for the heterostructures with normal band structures e.g [40] as well as with inverted band structures e.g [41]. The case of the pure HgTe is very well known but shows that the simply FDM method is very good tools for this purpose.

The different then (001) grow oriented structures can be calculated using the Hamiltoanin for zinc-blende structures presented in Ref. [19]. In the case of the 6nm HgTe QW (Fig. 4a) the difference between these two oriented structures in visible only for Γ_{lh} subband and only for k>0.1nm^{-1}. The bigger difference is observed for strained QW (Fig. 4b). Such wide structures is strongly investigated [42]. In this case the strained undirected energy gap is very small (<1meV) for 14 nm strained HgTe QW. It is worth to mention that the self-consistent potential is not included in presented results. Such potential can play an important role for the case when the undirect gap is so small like in the presented case.

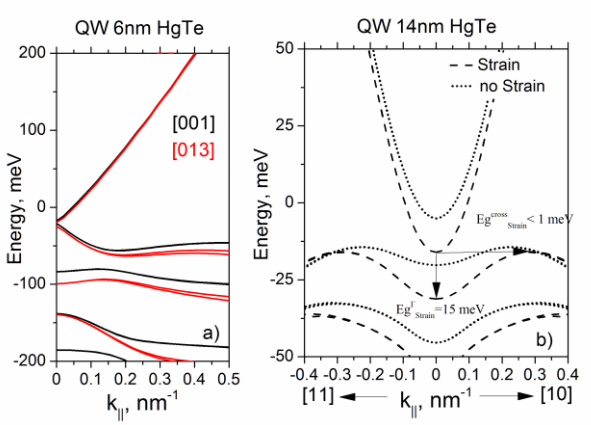

Fig. 4 . The dispersion relation for: a) 6nm wide HgTe QW for two different grow oriented structures- [001] and [013]; b) for strained and unstrained 14 nm wide HgTe QW.

The question is if it is possible to obtain a strained QW with Dirac point, and how does the dispersion relation look like in such cases. The answer is presented on Fig. 5b, where the $(E(k_{||})$ for a different HgTe QWs width was calculated for different mismatch levels of lattice constants so that each time a Dirac cone can be achieved for each QWs. The wider QW needs bigger lattice mismatch (see Fig. 5a), the bigger lattice mismatch caused that the light hole sub band is changes so for such structures with small concentration it is possible to observe the hole behaviour in for which the dispersion have Dirac like shape.

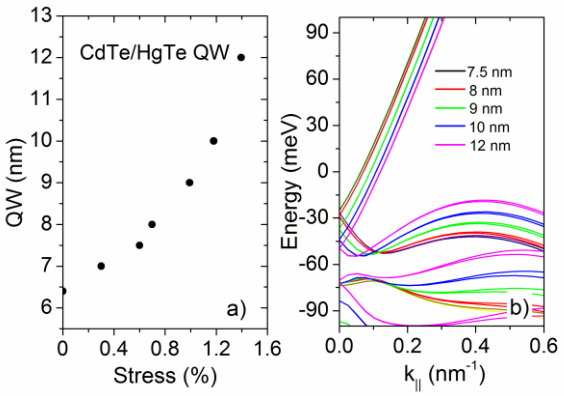

Fig. 5. a) the QW width as a function of the strain (lattice mismatch) for structures with Dirac point: b) The $E(k_{||})$ for a different HgTe QWs width was calculated for different mismatch levels of lattice constants so that each time a Dirac cone can be achieved for each QWs. The parameters of the lattice mismatch for the following QWs are equal: 0.32% for 7.5 nm wide QW, 0.40% for 8 nm wide QW, 0.70% for 9 nm wide QW, 0.98% for 10 nm wide QWand 1.20% for 12 wide nm QW.

The another possibility is to get the two dimensional Dirac like dispersion for mixed HgCdTe structures. For the case when the barrier area are build by HgCdTe it is possible to obtain the Dirac point but for the QW which are thinner then critical value 6.4nm for pure HgTe (see Fig. 6a). On the other hand, for the mixed material for QW the Dirac like dispersion for unstrained structures can be received for wider QW

structures – about 10nm for $Hg_{0.95}Cd_{0.05}Te$ QW and 17nm for $Hg_{0.9}Cd_{0.1}Te$ QW.

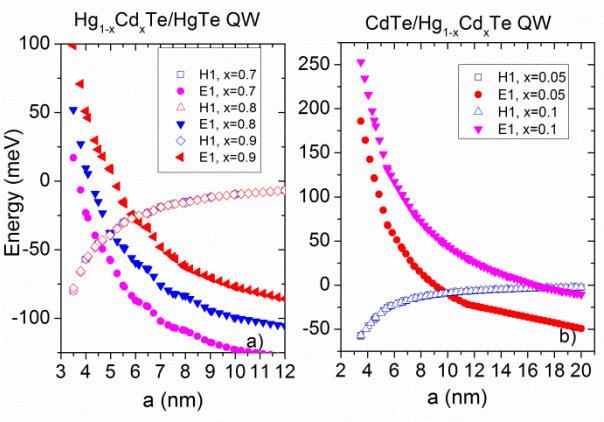

Fig. 6. Energy of the electron like subband (E1) and like – hole (H1) as a function of the widths the QW for: a) the different x-Cd compounds in the barrier material in HgCdTe/HgTe-QW and b) different x-cd compounds in the QW material in CdTe-HgCdTe QW.

3.2 3D strained systems

Dispersion relation calculated within an eight-band kp model at eight different x-Cd composition including strain for $Hg_{1-x}Cd_xTe$ layers 150 nm wide are presented in Fig. 7. In case of the HgTe (Fig. 7a)) the dispersion relation looks the same as in the other publications for the 75 nm wide structures [7,18]. It should be noted that because of hybridization with the valence-band states, the position of the Dirac point for HgTe is not directly obvious from the dispersion plot in the presented range - it is located at about -81 meV. In the presented cases the calculations were made for symmetric structures with two identical interfaces: $CdTe/Hg_{1-x}Cd_xTe$ and $Hg_{1-x}Cd_xTe/CdTe$ so there is no inversion symmetry break and the Dirac point does not split as it happens in case of two different interfaces.

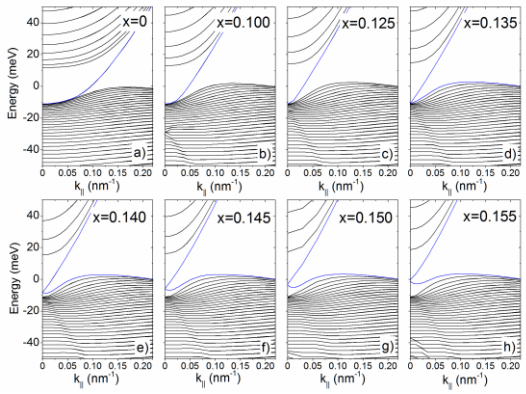

Fig. 7. Dispersion relation for 150 nm wide strained 3D $Hg_{1-x}Cd_xTe$ structures for x from 0 up to 0.155.

The position of the Dirac point goes up together with the increase of the x-Cd composition. For x=0.100 is located around -29 meV (Fig. 7b)), for the higher values of x Dirac point is located around the top of the valence band (for x=0.125 between -20 and -15 meV - Fig. 7c), and about -11 meV for x=0.135 - Fig. 7d). For the higher value of the x the Dirac point is being created inside the energy gap induced by the strain (Figs. 7e)-h)). For these values of the Cd composition the $Hg_{1-x}Cd_xTe$ is a true topological insulator. The information about the location of the Dirac cone in each cases can be inferred from the distribution of the charge carriers. As mentioned above, two identical interfaces are considered so there is one Dirac point as it can be seen in Figs. 7b) and 7c).

It can be clearly seen in Fig. 7 that for x>0.130 the energy of the surface states can be found in the fullest extent of the energy in the strained gap. For the x=0.155 the $\sum_{i=1}^{8}\Psi_i^2(z)$ were calculated (see Fig. 8) along $k_{||}$ for the energy dispersion region inside the strained gap which corresponds to $k_{||}$ from $k_{||}$ =0 up to $k_{||} = 0.06nm^{-1}$. The detailed description of the charge distribution in mixed $Hg_{1-x}Cd_xTe$ 3D TI is presented in Ref. [43].

The question is if it possible to obtain the Dirac point at the energy gap for 3D HgTe TI. Our previous calculation was done for 150 nm wide $Hg_{1-x}Cd_xTe$ structures with x=0.155 and 0.3% of the mismatch of the lattice constant due to the fact that for this type of structure, the Dirac point is in the middle of the strained gap - Fig. 8h.

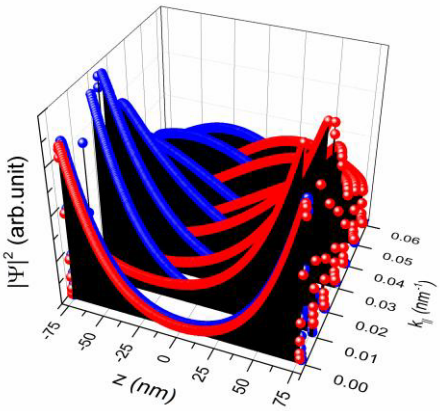

Fig. 8. $\sum_{i=1}^{8}\Psi_i^2(z)$ along $k_{||}$ for the energy dispersion region inside the strained gap which corresponds to $k_{||}$ from $k_{||}$ =0 up to $k_{||} = 0.06nm^{-1}$ for two energy states for the upper part of the Dirac cone (blue and red point respectively) from $E(k_{||} = 0) = 0$ meV up to $E(k_{||} = 0.06nm^{-1}) = 20$ meV for 150nm wide strained 3D $Hg_{0.845}Cd_{0.155}Te$.

The detailed analysis show that for the pure 3D HgTe 75nm wide TI it is possible to obtain the Dirac point inside of the strained gap only if the mismatch of the lattice constancy is equal at least 5% [43]. In the opposite to this the Dirac point inside of the strained gap can be found for mixed HgCdTe but the width of the structures has to be about 150 nm – for the narrower structures the gap between two Dirac cones appears and the charge distribution is typical like for the bulk.

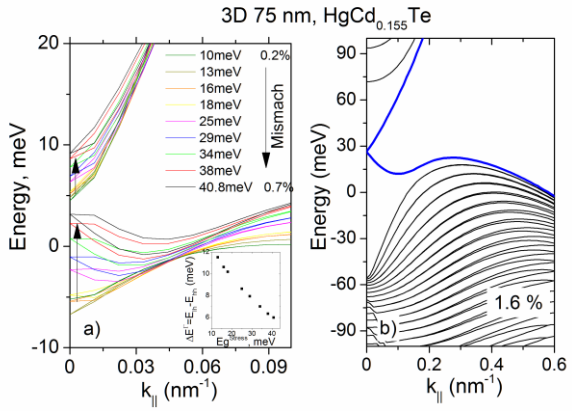

Fig. 9. a) $E(k_{||})$ for different lattice mismatch for 3D 75nm wide HgCd0.155Te (inset the difference between upper and lower Dirac cones as a function of the gap induced by strain is presented); b) the 75nm $HgCd_{0.155}Te$ wide 3D TI with lattice mismatch equal 1.6% - there is no gap between Dirac cones.

On Fig. 9 the analysis of the strained 75 nm wide $HgCd_{0.155}Te$ are presented. To get the graphene like dispersion in such structures it is necessary to applied the strain which can be realized by 1.6% lattice mismatch between substrate and 3D TI material (Fig. 9b). In other cases (smaller strain) (Fig. 9a) the gap between Dirac cones caused that the charge distribution is typical like for the bulk[43].

4 Summary

In the presented papers the results of the calculation the dispersion relation for mixed HgCdTe 2D and 3D structures are presented. The uniaxial tensile strain and the different x-Cd composition cause that obtained Dirac like dispersion in those cases can be achieve for different mixed heterostructures. For the 2D mixed $Hg_{1-x}Cd_xTe$ for different widths which is caused by the different level of the x-Cd compounds in the quantum well material as wells as in the barrier material the Dirac point can be found also. Our calculations show that it is possible to obtain the dispersion relation of the TSS for 3D 75 nm wide strained layers which looks similar to that one obtained for the strained HgCdTe/HgTe QW with the range width from 8 nm up to 9 nm. It happens if two conditions are fulfilled: the x-Cd composition should be equal about 0.155, and the level of the mismatch of the lattice constant should be about 1.6% (Fig. 7c). Then the Dirac point at the Γ-point is above the top of the Γ^8_{hh} band. The consequences of such shape of the dispersion relation of the TSS for the investigated 2D and 3D strained system are highly desirable. In the case of the 3D system the energy distance between Dirac point and the bottom of the Γ^8_{lh} is much greater than in case of the typical 3D HgTe TI and is over 40 meV. The shape of the lower part of the Dirac cone and its relative position to the Γ^8_{hh} states gives an opportunity for the experimental investigation of this TSS part as it is also for the strained 2D system. As shown by the other authors the theoretical and experimental investigation of both upper and lower part of the Dirac cones in case of the HgTe QW provides a lot of interesting results [44-48]. The 2D and 3D strained structures with the TSS dispersion relation similar to that obtained for HgTe QW should be a very interesting experimental object for further verification of all these effects.

This work was partly supported by the EU Foundation by the TARI-contract PRI-CT-1999-00088. We acknowledge support from the authorities of the Podkarpackie Voiwodership (Marshals O_ce of the Podkarpackie Voivodship of Poland), contract WNDPPK. 01.03.00-18-053/12

References

1. L. Fu, C. L. Mele, Phys. Rev. Lett. **94** (2007)
2. H. Zhang, C. X. Liu, X. L. Qi, X. Dai, Z. Fang and S. C. Zhang, Nature Physics **5**, 438-442 (2009)
3. D. Hsieh, D. Qian, L. Wray, Y. Xia, Y. S. Hor, R. J. Cava, M. Z. Hasan, Nature. **452**, 970-974. (2008)
4. Y. Xia, D. Qian, D. Hsieh, L. Wray, A. Pal, H. Lin, A. Bansil, D. Grauer, Y. S. Hor, R. J. Cava, M. Z. Hasan, Nature Physics. **5**, 398-402 (2009)
5. D. Hsieh, Y. Xia, D. Qian, L. Wray, F. Meier, J. H. Dil, J. Osterwalder, L. Patthey, A. V. Fedorov, H. Lin, A. Bansil, D. Grauer, Y. S. Hor, R. J. Cava, and M. Z. Hasan, Phys. Rev. Lett. **103,** 146401 (2009)
6. B. A. Bernevig, T. L. Hughes, S. C. Zhang, Science **314,** 1757 (2006)
7. M. Konig, S. Wiedmann, C. Brüne, A. Roth, H. Buhmann, L. W. Molenkamp, X. L. Qi, S. C. Zhang. Science **318,** 5851 (2007)
8. M. Konig, H. Buhmann, L. W. Molenkamp, T. L. Hughes, C.X. Liu, X. L. Qi, S. C. Zhang. J. Phys. Soc. Jap. **77,** 031007 (2008)
9. C. Brüne, C. X. Liu, E. G. Novik, E. M. Hankiewicz, H. Buhmann, Y. L. Chen, X. L. Qi, Z. X. Shen, S. C. Zhang, and L.W. Molenkamp. Phys. Rev. Lett. **106**, 126803 (2011)
10. D. A. Kozlov, Z. D. Kvon, E. B. Olshanetsky, N. N. Mikhailov, S. A. Dvoretsky, and D. Weiss. Phys. Rev. Lett. **112**, 196801 (2014)
11. K. M. Dantscher, D. A. Kozlov, P. Olbrich, C. Zoth, P. Faltermeier, M. Lindner, G. V. Budkin, S. A. Tarasenko, V. V. Belkov, Z. D. Kvon, N. N. Mikhailov, S. A. Dvoretsky, D. Weiss, B. Jenichen, and S. D. Ganichev. Phys. Rev. B. **92,** 165314 (2015)

12. M. Z. Hasan and C. L. Kane. Rev. Mod. Phys. **82**, 3045 (2010)
13. X. L. Qi and S. C. Zhang. Rev. Mod. Phys. **83,** 1057 (2011)
14. X. Dai, T. L. Hughes, X. L. Qi, Z. Fang, and S. C. Zhang. Phys. Rev. B. **77**, 125319 (2008)
15. C. X. Liu, X. L. Qi, H. J. Zhang, X. Dai, Z. Fang, and S. C. Zhang. Phys. Rev. B. **82**, 045122 (2010)
16. D. G. Rothe, R. W. Reinthaler, C. X. Liu, L. W. Molenkamp, S. C. Zhang and E. M. Hankiewicz. New Journal of Physics **12**, 065012 (2010)
17. R. L. Chu, W. Y. Shan, J. Lu, and S. Q. Shen. Phys. Rev. B. **83**, 075110 (2011)
18. C. Brune, C. Thienel, M. Stuiber, J. Bottcher, H. Buhmann, E. G. Novik, C. X. Liu, E. M. Hankiewicz, L. W. Molenkamp. Phys. Rev. X. **4**, 041045 (2014)
19. A. Pfeuffer-Jeschke, *Bandstruktur und landau-Niveaus quecksilberhaltinger II-VI-Heterostrukturen*, Universitt Wurzburg, Germany: Physikalisches Institut; (2000)
20. E. G. Novik, A. Pfeuffer-Jeschke, T. Jungwirth, V. Latussek, C. R. Becker, G. Landwehr, H. Phys. Rev. B. **72**, 035321 (2005)
21. S. A. Dvoretsky, D. G. Ikusov, Z. D. Kvon, N. N. Mikhailov, V. G. Remesnik, R. N. Smirnov, Yu. G. Sidorov, V. A. Shvets, *Semiconductor Physics, Quantum Electronics & Optoelectronics* **10**, 47-53 (2007)
22. G. Tomaka, J. Grendysa, P. Sliz, C. R. Becker, J. Polit, R. Wojnarowska, A. Stadler, E. M. Sheregii. Phys. Rev. B. **93**, 205419 (2016)
23. S. Wiedmann, A. Jost, C. Thienel, C. Brune, P. Leubner, H. Buhmann, L. W. Molenkamp, J. C. Maan, and U. Zeitler. Phys. Rev. B. **91**, 205311 (2015)
24. M. Orlita, D. M. Basko, M. S. Zholudev, F. Teppe, W. Knap, V. I. Gavrilenko, N. N. Mikhailov, S. A. Dvoretskii, P. Neugebauer, C. Faugeras, A. L. Barra, G. Martinez, M. Potemski, Nature Physics **10**, 233-238 (2014)
25. O. Crauste, Y. Ohtsubo, P. Ballet, P. A. Louis Delplace, D. Carpentier, C. Bouvier, T. Meunier, A. Taleb-Ibrahimi, L. Lévy. arXiv.:1307 (2008)
26. N. F. Johnson, H. Ehrenreich, P. M. Hui, P. M. Young. Phys. Rev. B. **41**, 3655 (1990)
27. L. R. Ram, K. H. Yoo, R. L. Aggarwal. Phys. Rev. B. **38**, 6151 (1988)
28. K. H. Yoo, L. R. Ram-Mohan, and D. F. Nelson. Phys. Rev. B. **39**, 12808 (1989)
29. D. C. Hutchings. Apply. Phys. Lett. **55**, 1082 (1989)
30. P. Harrison. *QuantumWells, Wires and Dots.* 2nd ed. Wiley, New York (2006)
31. K. Q. Le, *Microwave and Optical Technology Letters*. **51**, 1 (2009)
32. X. Ma, K. Li, Z. Zhang, H. Hu, Q. Wang, X. Wei, G. Song. Journal of Apply. Phys. **114**, 063101 (2013)
33. S. F. Tsay, J. C. Chiang, Z. M. Chau, I. Lo. Phyes. Rev. B. **56**, 13242 (1997)
34. J. D. Cooper, A. Valavanis, Z. Ikoni, P. Harrison, J. E. Cunningham. Apply. Phys. Lett. **108**, 113119 (2010)
35. Y. Jiang, X. Ma, Y. Xu, G. Song. Journal of Apply. Phys. **116**, 173702 (2014)
36. C. R. Becker, V. Latussek, A. Pfeuffer-Jeschke, G. Landwehr, L. W. Molenkamp. Phys. Rev. B. **62**, 10353 (2000)
37. L. D. Caro, L. Tapfer. Phys Rev. B. **51**, 4374 (1995)
38. G. L. Bir, G. E. Pikus. *Symmetry and Strain-Induced Effects in Semiconductors*. New York: Wiley; (1974)
39. A. Rogalski. Infrared Photon Detectors. Bellingham: SPIE Optical Engineering Press; (1995)
40. M. Zholudev, F. Teppe, M. Orlita, C. Consejo, J. Torres, N. Dyakonova, M. Czapkiewicz, J. Wróbel, G. Grabecki, N. Mikhailov, S. Dvoretskii, A. Ikonnikov, K. Spirin, V. Aleshkin, V. Gavrilenko, and W. Knap. Phys. Rev. B. **86**, 205420 (2012)
41. G. M. Minkov, A. V. Germanenko, O. E. Rut, A. A. Sherstobitov, S. A. Dvoretski, and N. N. Mikhailov. Phys. Rev. B. **93**, 155306 (2013)
42. E. B. Olshanetsky, Z. D. Kvon, G. M. Gusev, A. D. Levin, O. E. Raichev, N. N. Mikhailov, and S. A. Dvoretsky. Phys. Rev. Lett. **114**, 126802 (2015)
43. M. Marchewka, Physica E. **84**, 407-414 (2016)
44. M. V. Durnev and S. A.Tarasenko. Phys. Rev. B. **93**, 075434 (2016)
45. G. M. Minkov, A. V. Germanenko, O. E. Rut, A. A. Sherstobitov, M. O. Nestoklon, S. A. Dvoretski, and N. N. Mikhailov. Phys. Rev. B. **93**, 155304 (2016)
46. S. A. Tarasenko, M. V. Durnev, M. O. Nestoklon, E. L. Ivchenko, J.W. Luo, and A. Zunger. Phys. Rev. B. **91**, 081302(R) (2015)
47. O. E. Raichev, G. M. Gusev, E. B. Olshanetsky, Z. D. Kvon, N. N. Mikhailov, S. A. Dvoretsky, and J. C. Portal. Phys. Rev. B. **86**, 155320 (2012)
48. M. Pang and X. G. Wu. Phys. Rev. B. **88**, 235309 (2013)